

Intrinsically Episodic Antarctic Shelf Intrusions of Circumpolar Deep Water via Canyons[©]

ELLIE Q. Y. ONG^D,^a EDWARD DODDRIDGE,^b NAVID C. CONSTANTINO^c, ANDREW MCC. HOGG,^c AND MATTHEW H. ENGLAND^d

^a Climate Change Research Center, Australian Center for Excellence in Antarctic Science and Australian Research Council Center of Excellence for Climate Extremes, University of New South Wales, Sydney, New South Wales, Australia

^b Australian Antarctic Program Partnership, Institute for Marine and Antarctic Studies, University of Tasmania, Nipaluna/Hobart, Tasmania, Australia

^c Research School of Earth Sciences and Australian Research Council Center of Excellence for Climate Extremes, Australian National University, Canberra, Australian Capital Territory, Australia

^d Centre for Marine Science and Innovation and ARC Australian Center for Excellence in Antarctic Science, University of New South Wales, Sydney, New South Wales, Australia

(Manuscript received 21 April 2023, in final form 1 February 2024, accepted 8 March 2024)

ABSTRACT: The structure of the Antarctic Slope Current at the continental shelf is crucial in governing the poleward transport of warm water. Canyons on the continental slope may provide a pathway for warm water to cross the slope current and intrude onto the continental shelf underneath ice shelves, which can increase rates of ice shelf melting, leading to reduced buttressing of ice shelves, accelerating glacial flow and hence increased sea level rise. Observations and modeling studies of the Antarctic Slope Current and cross-shelf warm water intrusions are limited, particularly in the East Antarctica region. To explore this topic, an idealized configuration of the Antarctic Slope Current is developed, using an eddy-resolving isopycnal model that emulates the dynamics and topography of the East Antarctic sector. Warm water intrusions via canyons are found to occur in discrete episodes of large onshore flow induced by eddies, even in the absence of any temporal variability in external forcings, demonstrating the intrinsic nature of these intrusions to the slope current system. Canyon width is found to play a key role in modulating cross-shelf exchanges; warm water transport through narrower canyons is more irregular than transport through wider canyons. The intrinsically episodic cross-shelf transport is found to be driven by feedbacks between wind energy input and eddy generation in the Antarctic Slope Current. Improved understanding of the intrinsic variability of warm water intrusions can help guide future observational and modeling studies in the analysis of eddy impacts on Antarctic shelf circulation.

KEYWORDS: Antarctica; Continental shelf/slope; Eddies; Ocean dynamics; Idealized models; Ocean models

1. Introduction

The Antarctic Slope Current (ASC) is a westward-flowing current around Antarctica, lying close to the coast over the continental slope (Thompson et al. 2018). The ASC is closely coupled to the Antarctic Slope Front, which is characterized by steeply sloping isopycnals located over the Antarctic continental slope, spinning up a westward geostrophic current between the saline open ocean and the fresher Antarctic continental shelf. A key water mass of the saline open ocean is the Circumpolar Deep Water (CDW) (e.g., Heywood et al. 2014; Thompson et al. 2018; Morrison et al. 2020; Daee et al. 2020). The poleward transport of this warm CDW is regulated by the slope current; depending on the local structure of the ASC, CDW can intrude onto the continental shelf, transporting heat poleward to the Antarctic shelf. This process can induce basal melt of ice shelves and increase glacial and ice sheet flow, resulting in global sea level rise (Depoorter et al. 2013; Hattermann et al. 2014; Herraiz-Borreguero et al. 2016;

Rintoul et al. 2016; DeConto and Pollard 2016; Gudmundsson et al. 2019).

Given the significant impact Antarctic ice shelf melt can have globally, the extent to which CDW intrudes underneath the ice shelves of the East Antarctic Ice Sheet is a major concern. The East Antarctic Ice Sheet holds a total sea level equivalent of ~50 m, an order of magnitude larger than that of the West Antarctic Ice Sheet (Stokes et al. 2022). However, much less research has been conducted in the East Antarctic compared to the West Antarctic region (Morlighem et al. 2020; Stokes et al. 2022). The East Antarctic Ice Sheet has previously been thought to be stable, with landlocked sectors that are not directly impacted by CDW intrusions and past melt rates that have been lower than those in the West Antarctic (e.g., Paolo et al. 2015; Stokes et al. 2022). However, recent studies point toward a greater mass loss than previously predicted, especially in marine-based sectors of the East Antarctic Ice Sheet exposed to CDW intrusions onto the continental shelf (e.g., Rignot et al. 2019; Stokes et al. 2022), highlighting the vulnerability of the East Antarctic Ice Sheet to melting due to warm water intrusions.

The sloped isopycnals of the ASC in East Antarctica are generally thought to act as a barrier between CDW offshore and the continental shelf; however, the presence of canyons in the topography on the continental shelf may provide a pathway for CDW flow onto the shelf. Oceanic observations have shown the presence of warm CDW intrusions through canyons in East Antarctica

[©] Supplemental information related to this paper is available at the Journals Online website: <https://doi.org/10.1175/JPO-D-23-0067.s1>.

Corresponding author: Ellie Q. Y. Ong, ellie.ong@unsw.edu.au

(Rintoul et al. 2016; Nitsche et al. 2017; Silvano et al. 2018, 2019; Hirano et al. 2020; Ribeiro et al. 2021; Herraiz-Borreguero and Naveira Garabato 2022). However, our physical understanding of these warm CDW intrusions via canyons is incomplete, as observations are scarce (e.g., Peña-Molino et al. 2016; Herraiz-Borreguero et al. 2016) and modeling studies are also limited, as outlined below. Our understanding of canyons' effect on warm water intrusions is also limited by the limited bathymetric measurements around the East Antarctic margin (Nitsche et al. 2017; Silvano et al. 2019; McMahon et al. 2023), which show many discrepancies between observations and bathymetric products. There is, however, a better understanding of shelf intrusions via canyons outside of East Antarctica, where some previous work has investigated mechanisms inducing an onshore flow in the presence of a slope current. Possible drivers of onshore flow include steering of a shelf-break jet following strong canyon topography (Williams et al. 2001), mean flow-topographic interactions inducing a cyclonic circulation in the canyon (St-Laurent et al. 2013; Fennel and Schmidt 1991), or wave-topographic interactions under a jet residing further offshore (Zhang et al. 2011; St-Laurent et al. 2013). Another study has also investigated the effect of a continental slope on slope current variability, but this did not include the effect of a canyon (Stern et al. 2015). Hence, limited understanding of the effect of canyons on cross-slope CDW transport in the East Antarctic continental margin is a key motivation behind this research.

Existing modeling studies do not generally take into account all the key factors that influence how CDW intrusions occur on the East Antarctic continental shelf. Namely, these studies do not generally resolve eddies, canyons, and East Antarctica in the same model. Many regional modeling studies of the East Antarctic continental margin are not fully eddy-resolving (e.g., Gwyther et al. 2014, 2018; Nakayama et al. 2021), even though eddies are crucial in governing the transport of CDW onto the continental shelf (Nøst et al. 2011; Thompson et al. 2014; Stewart and Thompson 2015; Boeira Dias et al. 2023). To resolve eddies at the Antarctic continental margin, an order of ~ 500 m–1 km resolution is required to resolve a continental shelf Rossby radius of deformation of ~ 4 km (which corresponds to a $1/48^\circ$ resolution) (St-Laurent et al. 2013; Stewart and Thompson 2015). Conversely, existing eddy-resolving studies do not generally investigate the East Antarctic region and the associated “fresh shelf regime,” where strong easterly winds result in the poleward Ekman transport of cool, surface water, the incropping of density surfaces, and a strong ASC (e.g., Thompson et al. 2018). Instead, eddy-resolving modeling studies, such as the ones by Daae et al. (2017) and Liu et al. (2017), generally focus on “dense shelf regime” regions of the Antarctic margin, where dense shelf water formation leads to the formation of Antarctic Bottom Water (e.g., Williams et al. 2010; Ohshima et al. 2013). These dense shelf water formation regions have different circulation regimes and dynamics compared to most of the East Antarctic margin (Darelius et al. 2014, 2016; Daae et al. 2017; Morrison et al. 2020); in particular, the dense shelf regime has an additional bottom-intensified slope current linked to dense shelf water export, which is independent of the surface-intensified current of the fresh shelf regime (Huneke et al. 2023). The only eddy-resolving modeling study of the fresh shelf regime is that by Liu et al. (2022), who investigate CDW intrusions via canyons,

focusing on the mechanisms of cross-shelf exchange in a single topographic configuration. Liu et al. (2022) find that warm water intrusions are steered onshore by the bottom pressure torque when the CDW flow first interacts with the mouth of the trough, with topographic Rossby waves driving a high-frequency variability of ~ 1 month. Currently, there are no eddy-resolving modeling studies investigating the effect of canyon width and geometry on the ASC and CDW intrusions in a fresh shelf regime; hence, our understanding of CDW intrusions under different canyon topographies remains poor. Addressing this question is therefore the focus of the present study.

Here, we explore warm CDW intrusions through canyons in an idealized channel configuration based on the East Antarctic continental margin, using a range of canyon configurations. We model the fresh shelf regime dominant around the East Antarctic margin using an idealized eddy-resolving primitive equation model with isopycnal coordinates. The isopycnal channel model is forced by wind stress at the surface, with restoring boundary conditions to the north. Using isopycnal coordinates allows us to model the stratification of the ASC with few vertical layers at a minimal computational cost, which makes it feasible to explore the parameter space of canyon geometries in eddy-resolving simulations. Further details about the isopycnal channel model setup are given in section 2. In section 3, we investigate the intrinsically episodic intrusions of CDW onto the shelf in the idealized channel simulations, showing the effect of canyon geometry on the regularity of these intrusions, and that the episodic variability of intrusions is linked to an intrinsic temporal variability of the ASC itself. In section 4, we examine the emergent intrinsic temporal variability of the ASC and develop a simplified low-order model, comprising two nonlinear ordinary differential equations, that is able to reproduce episodic ASC variability based on energy exchanges between different reservoirs. In section 5, we discuss the implications of our results and future work.

2. Model setup

The primary experiments in this study utilize an isopycnal channel model of the ASC to investigate the effect of different canyon configurations on CDW intrusions. We also develop, and later introduce in section 4, a low-order model of two ordinary differential equations that explains an emergent variability in ASC strength found in the isopycnal channel model. Section 2 will outline the setup of the primary isopycnal channel model and the experiments that were run to understand CDW intrusions across different canyon configurations.

The isopycnal channel model domain and forcings are designed to reproduce the fresh shelf regime (Thompson et al. 2018) and are inspired by the configuration used by Constantinou and Hogg (2019). We use the Modular Ocean Model, version 6 (MOM6) (Adcroft et al. 2019), to solve the hydrostatic Boussinesq primitive equations in isopycnal coordinates. We have a zonally reentrant channel on a beta plane, with a zonal extent of 1000 km, meridional extent of 500 km, and maximum depth of 3 km, that includes topography of a continental slope. The height of the continental slope, from the top of the sill on the edge of the continental shelf to the bottom, is 2.5 km. The Coriolis parameter is $f = f_0 + \beta y$, with $f_0 = -10^{-4} \text{ s}^{-1}$, $\beta = 1.5 \times 10^{-11} \text{ m}^{-1} \text{ s}^{-1}$ and

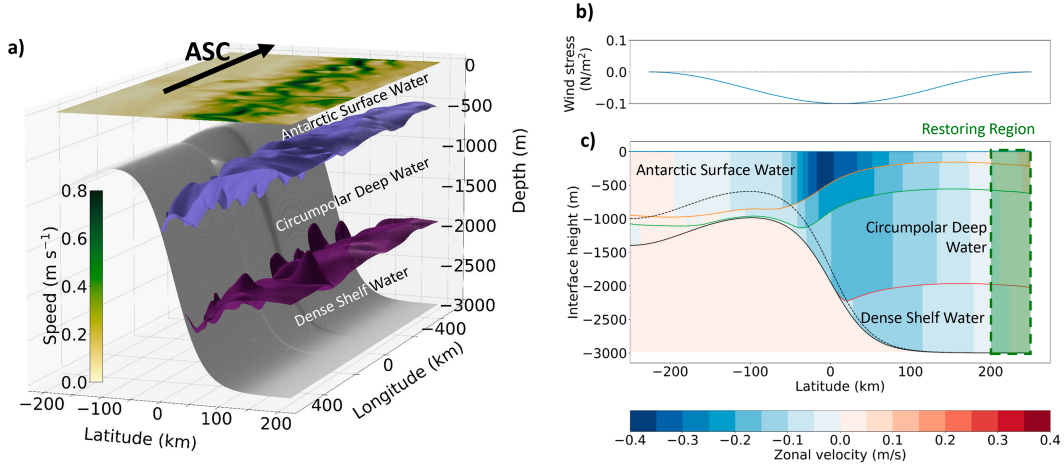


FIG. 1. (a) Snapshot of isopycnal interfaces for the upper surface water, CDW, and dense shelf water layers in the control simulation of the ASC, with the widest steep-sided canyon topography. Instantaneous surface speed is shown on the top isopycnal interface. (b) Profile of zonal wind stress forcing, applied at the surface. (c) The cross-sectional profile of isopycnal surfaces in the center of the canyon between each of the four density layers: upper and lower surface water, CDW, and dense shelf water. Colors in each density layer represent the 10-yr mean zonal velocity in each layer. The black dashed line shows the topography of the continental slope away from the canyon, while the black solid line shows the topography of the continental slope at the center of the canyon. The restoring region where density interfaces are relaxed to a set height at the northern boundary, representing the open ocean, is shown in green. The densities of each isopycnal layer are, starting from the surface layer, $\rho_1 = 1027.8 \text{ kg m}^{-3}$, $\rho_2 = 1028.0 \text{ kg m}^{-3}$, $\rho_3 = 1028.1 \text{ kg m}^{-3}$, and $\rho_4 = 1028.3 \text{ kg m}^{-3}$.

with y the distance from the center of the channel in the latitudinal direction. These values are typical of the Southern Ocean, but the gradient in planetary vorticity has a smaller contribution to the dynamics than the effective beta induced by topography. Momentum is removed from the bottom isopycnal layer via quadratic drag with a drag coefficient of $c_{\text{drag}} = 0.003$.

The idealized channel model configuration is informed by the neutral density profiles and zonal velocities of sections of the ASC from global ocean–sea ice model simulations using the 1° Australian Community Climate and Earth-System Simulator Ocean Model, version 2.0 (ACCESS-OM2-01) global ocean–sea ice model and from previous idealized experiments (Stewart and Thompson 2015, 2016; Huneke et al. 2019; Kiss et al. 2020). We use four density layers to represent the slope current region: two layers of Antarctic Surface Water, a CDW layer, and a Dense Shelf Water layer. The density values used in each of the layers are $\rho_1 = 1027.8 \text{ kg m}^{-3}$, $\rho_2 = 1028.0 \text{ kg m}^{-3}$, $\rho_3 = 1028.1 \text{ kg m}^{-3}$, and $\rho_4 = 1028.3 \text{ kg m}^{-3}$ and were based on neutral density values from Stewart and Thompson (2015). The model domain is shown in Fig. 1a, with a snapshot of the top surface water isopycnal layer, CDW layer, and dense shelf water layer. There are no tides or other water mass transformations. The idealized isopycnal channel model is not able to model water mass transformations, such as the dense shelf water formation in regions characterized by a dense shelf regime, or basal melt in warm shelf regions in both West and East Antarctica. However, there are no water mass transformations in the fresh shelf regime if warm CDW has not yet intruded onto the continental shelf (Boeira Dias et al. 2023), enabling us to use this isopycnal channel framework to study episodic canyon intrusions in a fresh shelf regime. Density interfaces

are restored at the northern boundary to mimic the open ocean, with the depth of density interfaces at the northern boundary being prescribed in the initial conditions. The initial conditions are motivated by the fresh shelf regime modeled in the work by Stewart and Thompson (2015). The density interfaces throughout the rest of the domain are allowed to vary. The constant wind forcing spins up a current which subsequently becomes unstable and gives rise to eddies. The experiments are run until statistical equilibrium is reached. The initial stratification (before spinup) has a first Rossby deformation radius of 5 km on the shelf and 11 km offshore; thus, eddies are comfortably resolved by our simulations which have a 1-km lateral resolution. We experimented with a 2-km resolution configuration, but it did not fully resolve the eddying behavior in the ASC. A preliminary test on doubling the resolution to 0.5 km showed little qualitative change in ASC transport and CDW intrusions.

The wind stress forcing is steady and zonally symmetric, with only zonal wind forcing. We use a maximum wind stress input of $\tau_0 = 0.1 \text{ N m}^{-2}$ for the control simulation, as in the idealized configuration representing the fresh shelf regime in Stewart and Thompson (2015). The zonal wind stress τ_x is

$$\tau_x = -\tau_0 \cos^2(\pi y / \sigma_\tau), \quad (1)$$

where $\sigma_\tau = 500 \text{ km}$ is the width of the channel, also the width of the wind stress forcing profile. The zonal wind profile for the control simulation is shown in Fig. 1b. There is no seasonal variation in either the surface wind or northern boundary restoring forcing, and no sea ice model is incorporated in this channel configuration of MOM6.

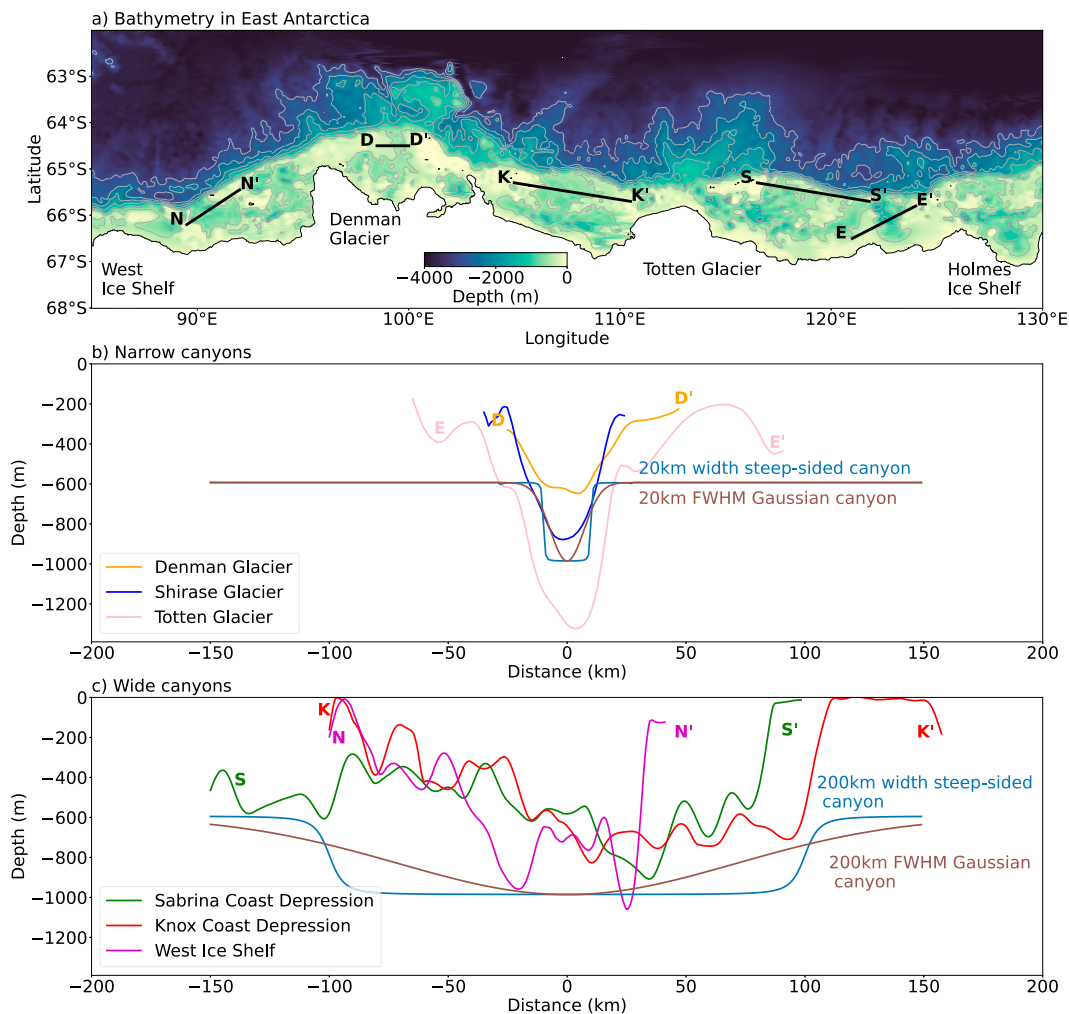


FIG. 2. (a) Observed bathymetry in the East Antarctic, using ETOPO1 data (NOAA National Geophysical Data Center 2009), with sampled canyon cross sections marked in black. Contours of 500-, 1000-, 1500-, and 2000-m depth are marked in gray. (b) Cross sections of observed narrow canyons taken from (a), labeled by name or associated glacier. The Shirase Glacier canyon at 38°–39°E is not shown in (a) as it is west of the domain pictured. Cross sections of idealized narrow canyons are shown in the steep-sided (blue) and Gaussian (brown) shapes. (c) Cross sections of observed wide canyons taken from (a), labeled by name or associated glacier. Cross sections of idealized wide canyons are shown in the steep-sided (blue) and Gaussian (brown) shapes.

We add canyons to the continental slope topography to investigate how their presence influences shoreward transport of CDW onto the continental shelf (see Fig. 2). The canyon geometries in this investigation are idealized: we use a steep-sided canyon, shaped like a trough with a relatively flat bottom in the canyon, or a canyon with sloped sides of a Gaussian shape (see blue and brown lines, respectively, in Figs. 2b,c). Figure 1a shows the topography for a steep-sided canyon of 200-km width. Simulations for the steep-sided and Gaussian canyon cases were run using canyons of width 20, 50, 100, 150, and 200 km at half of the canyon's maximum depth (analogous to the full width at half maximum) and with a canyon depth of 400 m relative to the continental shelf. The widths of the canyons are comparable to cross-sectional widths of canyons observed around the Antarctic margin, as shown in Fig. 2, and were chosen from the 1-min gridded

elevations/bathymetry for the world (ETOPO1) Global Relief Model (NOAA National Geophysical Data Center 2009). The topography of the continental slope is based on previous idealized experiments and the ACCESS-OM2-01 model (Stewart and Thompson 2015; Kiss et al. 2020).

After channel model spinup and equilibration, a snapshot of the stratification of the idealized fresh shelf regime is shown in Fig. 1a, for the control simulation with the steep-sided canyon of 200-km width, the widest canyon modeled. This stratification is comparable to observations, such as the section of the Eastern Weddell Sea in Fig. 3d of Thompson et al. (2018), who used data from Heywood and King (2002). Statistical equilibrium was typically reached after 20 years of spinup, with daily mean data for analysis taken from at least a 20-yr-long period of statistical equilibrium; each experiment is spun up separately. A strong

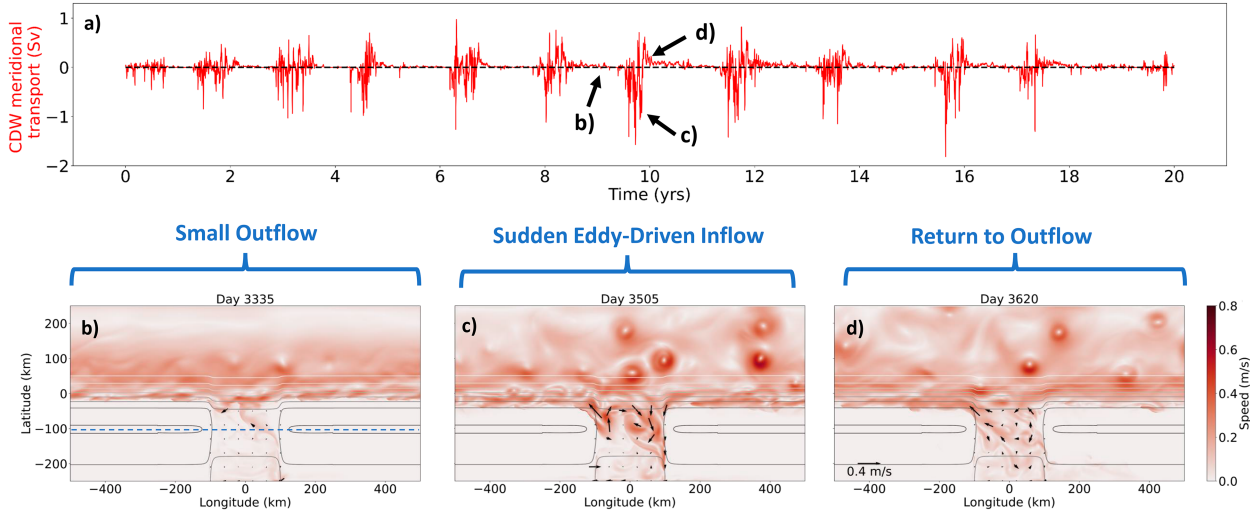


FIG. 3. (a) Meridional transport of CDW across a cross section of canyon at latitude $y = -100$ km in the control simulation over 20 years at equilibrium. The cross section is taken across the blue dashed line in (b). Snapshots of speed in the CDW layer of simulation showing representative examples of the different stages of episodic CDW intrusion: (b) a small outflow of CDW flowing off the continental shelf, (c) a sudden eddy-driven inflow onto the continental shelf, and (d) a return to a CDW outflow. We see that eddies form in the ASC and drive a large onshore flow approximately every 2 years. The eddies on the continental shelf then begin to dissipate and flow offshore, continuing on the cycle of CDW intrusions. A video showing the episodic CDW intrusions in this experiment is included in the online supplemental material.

westward current is spun up in the surface layers with a maximum zonal velocity of 0.3 m s^{-1} in the water column, when averaged over 10 years, shown in Fig. 1c. ASC velocities in this simulation are slightly higher than velocities in other models and observations. For example, Huneke et al. (2022) showed a maximum zonal velocity of 0.2 m s^{-1} in the water column in a region of the fresh shelf regime, when averaged over 10 years, while a regional model of the ASC showed maximum instantaneous zonal velocities off the Totten Ice Shelf in East Antarctica to be 0.2 m s^{-1} (Nakayama et al. 2021). In our simulation, density surfaces are steeply sloped and incroped into the continental slope, consistent again with regions in the fresh shelf regime. Although idealizations are made in the configuration so that eddies can be resolved and a wide parameter space can be explored, this control simulation still exhibits the key features characteristic of the fresh shelf regime and East Antarctica and is used as a basis for exploring how CDW intrusions access the Antarctic continental shelf through canyons.

3. Temporal variability of CDW intrusions and the ASC

We start by looking at the qualitative behavior of on-shelf intrusions in the control isopycnal channel simulation of Fig. 1. We choose the control simulation as this is the canyon configuration which allows for the largest CDW intrusions, and it typifies canyon geometry at certain locations around the East Antarctic sector (Fig. 2c). We are primarily interested in meridional transport of CDW; hence, the time series in Fig. 3a shows meridional transport in the CDW layer at the sill latitude across a section of the canyon (see dotted line in Fig. 3b), with poleward transport shown as negative. Since there is no water mass transformation

on the shelf, the CDW shelf exchange is balanced over a long time period. However, this time series shows that there is poleward meridional transport of CDW in the canyon and that this cross-shelf transport is not constant but instead occurs in isolated episodes approximately every 2 years. The different stages of CDW intrusion are highlighted in snapshots of speed in the CDW layer over time, shown in separate stages of Figs. 3b–d. The most common state of the system is the small outflow state of little cross-shelf exchange as indicated in Fig. 3b, with a minimal amount of CDW draining off the continental shelf. There is then a transition to a stronger eddy field in the ASC, corresponding with a stage of sudden eddy-driven flow of CDW onshore, with coherent vortices reaching the continental shelf as seen in Fig. 3c. While CDW pools on the continental shelf, eddies in the ASC weaken, and CDW begins to flow offshore, returning to the original state of primarily offshore transport of CDW as indicated in Fig. 3d. This entire cycle of weak CDW offshore flow, followed by a sudden shoreward flow, and a return to an offshore flow is surprising given that the simulated ASC has reached a statistically steady state. Additionally, as wind and sponging of layer interfaces remain constant throughout the simulation, this interannual variability of episodic CDW intrusions is not the result of external forcings, pointing to the presence of intrinsic temporal variability. Previous studies have all focused on the initial driver of CDW intrusions: St-Laurent et al. (2013), for example, showed that wave-topographic interactions allowed for a steady anticyclonic circulation in the canyon to develop in an idealized model of the Marguerite Trough of the Bellingshausen Sea. However, no previous work has pointed to mechanisms driving an intrinsic variability in CDW intrusions independent of external forcings. Understanding this CDW transport variability is the focus of the

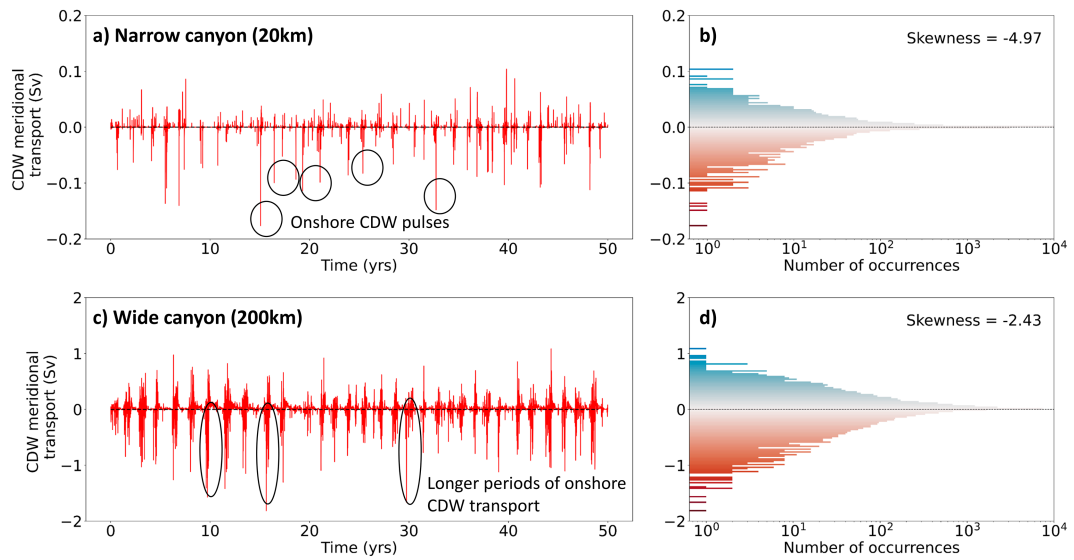


FIG. 4. (a) Meridional transport of CDW across latitude $y = -100$ km and (b) probability density function of meridional transport of CDW across the same latitude for the narrow 20-km-wide steep-sided canyon case. (c),(d) As in (a) and (b), respectively, but for the wide 200-km steep-sided canyon case. Skewness values of meridional CDW transport indicate that a more negatively skewed distribution has more irregular and episodic CDW intrusions. The peaks circled show examples of isolated pulses of CDW onshore in (a) and longer periods of intrusions in (c). The colors in the probability distribution function of (b) and (d) qualitatively represent CDW flowing onshore and heating the shelf in red and CDW leaving the shelf in blue.

rest of this section, initially analyzing the effect of canyon width on the variability of CDW intrusions and then investigating the origins of the CDW variability.

a. Effect of canyon width on warm water intrusions

We observe in the control simulation the intrinsically episodic behavior of CDW intrusions through a canyon and see in Fig. 3 that the canyon is a key pathway by which CDW reaches the continental shelf. Hence, we aim to understand how the characteristics of the canyon, specifically the width of the canyon, affect the episodic poleward flow of CDW. We first compare the narrowest (20-km width) and widest (200-km width) steep-sided canyon cases of the simulations we have run. The time series of meridional CDW transport at the sill latitude is plotted in Fig. 4, with the time series for the narrow canyon case in Fig. 4a and that of the widest canyon case in Fig. 4c. Qualitatively, the narrower canyon case shows more isolated instances of CDW intrusions highlighted by circles in Fig. 4a. However, CDW intrusions in the wider canyon case last for a longer period of time, instead of the isolated single bursts of CDW traveling onto the shelf in the narrow canyon case, shown in the ovals in Fig. 4c. A plot of the probability density function for meridional CDW transport using 50 years of daily data reveals isolated pulses of large poleward transports in the narrow canyon case (Fig. 4b for the narrow 20-km and Fig. 4d wide 200-km case). The isolated pulses of CDW in the narrow canyon case are separated from the central distribution, causing the distribution to be heavily skewed. Hence, a topographic configuration with more asymmetric, or irregular, CDW intrusions has a more negatively skewed distribution of meridional CDW transport.

To directly compare the regularity of CDW transport across different canyon widths, we use the Fisher-Pearson coefficient of skewness to quantify the asymmetry of CDW flow on and off the shelf. The results of this comparison are shown in Fig. 5a, plotting the skewness, analogous to the regularity of intrusion, against the hydraulic area of the canyon. Skewness calculations at each canyon configuration use four subsampled sections of 20-yr-long time series, overlapping by 10 years, from which a median skewness is calculated. For the narrowest canyons, a few isolated intrusion events cause a large spread in skewness. Therefore, to increase the robustness of the skewness metric, we run the smallest two Gaussian canyons and the narrowest steep-sided canyon cases longer for a 70-yr-long statistically equilibrated time series, improving the skewness statistics with two more subsampled sections. We use skewness as a metric because simulations with smaller canyons have increasingly rare onshore CDW transport events, reflected in a more negatively skewed distribution. We have defined the hydraulic area to be the cross-sectional area of the canyon at the shelf break, at the latitude $y = -100$ km. For the steep-sided canyon experiments (orange line), we find that narrower canyons have a more negatively skewed distribution of meridional CDW transport and thus more asymmetric CDW transport. Narrow steep-sided canyons have sudden large intrusions but more frequent instances of small CDW drainage, while wider steep-sided canyons exhibit less asymmetry between the CDW drainage and intrusions onto the shelf. Hence, the frequency of CDW flow onshore is relatively steady in wide canyons, which can improve the predictability of intrusions. Observed canyons do not always have geometries comparable to the steep-sided case, so we conducted the same analysis for experiments

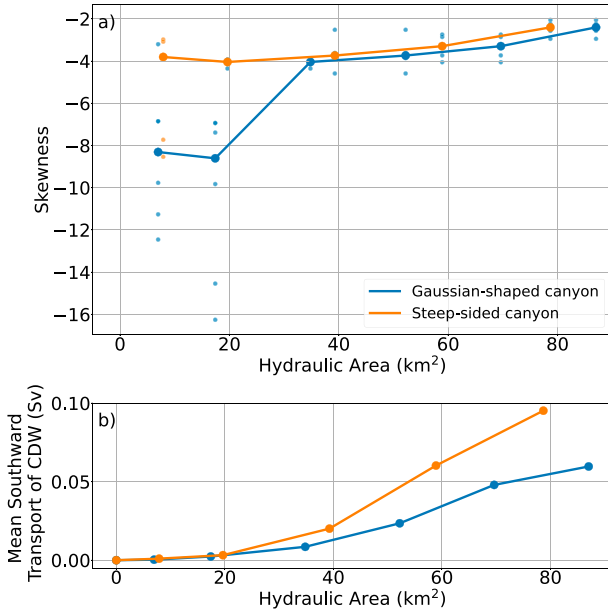


FIG. 5. (a) Skewness of meridional CDW transport distribution as in Fig. 4 with the hydraulic area of canyon, for canyons of steep-sided and Gaussian shapes. Skewness calculations for each canyon configuration use subsampled sections of 20-yr length, overlapping by 10 years. The low-opacity, smaller points are skewness values for subsampled sections, while the median skewness values for each canyon configuration are plotted in the solid color. Narrower canyons have a more negatively skewed distribution, with greater asymmetry and irregularity in CDW transport. For the two smallest Gaussian canyons and the narrowest steep-sided canyon cases, we run experiments for 70 years instead of 50 years, to improve the statistics in narrow canyons with irregular onshore flow. (b) Mean southward transport of CDW across latitude $y = -100$ km with the hydraulic area of canyon for canyons of steep-sided and Gaussian shapes. Canyons with a larger hydraulic area allow for a greater transport of CDW poleward and more regular intrusions.

with canyons of a more gently sloped Gaussian shape with varying widths, plotted in blue in both panels of Fig. 5, where we confirm that the same overall trend in episodic behavior with canyon width holds as in the steep-sided canyon cases. Note that additional experiments run with wind forcing shifted north/south by 50 km reveal that the skewness is more sensitive to canyon geometry than modest shifts in ASC position.

Alongside understanding the nature of CDW intrusions and its variability, we also compare poleward CDW transport between different canyon configurations. We select the southward transport values of CDW at the sill latitude, zero out any northward transport, and zonally integrate the southward transport at each time step before taking the temporal mean over 50 years of daily data. The time-mean southward transport of CDW is computed in simulations with a range of canyon widths and canyon geometries, including a simulation without a canyon on the continental slope, as seen in Fig. 5b. Across both canyon geometries, southward transport of CDW onto the shelf increases with the hydraulic area available for flow onto the shelf. Note that in the simulation without a canyon, there is no southward transport

of CDW across the sill latitude, highlighting the importance of canyons in CDW intrusions. Additionally, canyon configurations with steep-sided canyons have a greater southward transport of CDW than those with a Gaussian shape shown in blue in Fig. 5b, even when canyons with the same hydraulic area are compared. We conclude that wider canyons allow for more CDW transport onto the shelf, with less asymmetry in meridional CDW transport when compared to narrower canyons, and this result is robust for the two canyon geometries tested.

The effect of canyon width on the regularity of CDW intrusions can affect the predictability of the East Antarctic Margin: although narrow canyons allow for less CDW transport poleward, the asymmetry toward intrusions and the key locations of narrow canyons, e.g., beneath the Denman Glacier, may indicate that further study into cross-shelf dynamics across narrow canyons is required in order to predict the variability of warm water intrusions onto the shelf where vulnerable ice shelves sit. Wider canyons allow for greater CDW transport, with intrusions occurring periodically at a set frequency, which may make flow at these wider canyons easier to predict. We next investigate the mechanisms governing the periodic behavior of CDW intrusions.

b. Link between CDW intrusions and ASC variability

Although we have found an intrinsic temporal variability of CDW intrusions across a range of canyon geometries, the mechanisms governing the variability are unclear. We can nonetheless see a connection between the variability of CDW intrusions and the ASC strength in Fig. 6a, where the strength of the ASC is plotted in blue and the meridional CDW transport in red, both plotted for 20 years at statistical equilibrium. In the control simulation with the widest canyon, the ASC strength varies from 40 to 80 Sv ($1 \text{ Sv} \equiv 10^6 \text{ m}^3 \text{ s}^{-1}$) with a mean of around 60 Sv, larger than the ASC strengths observed by Peña-Molino et al. (2016), which varies between 0 and 100 Sv of westward transport with a mean of around 20 Sv. The ASC strength exhibits variability on an interannual time scale, and in this control simulation, the poleward transport of CDW is maximized when the slope current is weaker.

The simulated interannual variability in the ASC is unlike those observed in existing studies. Regional simulations of the Totten Glacier region with time-varying external wind forcings have previously shown a temporal variability in ASC strength, with strong ASC weakening events occurring about every 10 years but also a higher-frequency variability on the order of years (Nakayama et al. 2021). Direct observations of the ASC in East Antarctica have instead primarily found higher-frequency variability in ASC strength (Peña-Molino et al. 2016); however, these observed time series are shorter than 2 years, which would not be sufficient to capture biennial oscillations in ASC strength. However, an increased poleward transport of CDW under a weakened ASC is consistent with the results by Nakayama et al. (2021) and posits a link between episodic warm water intrusions and the ASC strength.

Most relevant to fresh shelf regime regions around East Antarctica, intrusions of warm water onto the Antarctic continental shelf have previously been found to be driven by eddy activity (Nøst et al. 2011; St-Laurent et al. 2013; Hattermann et al. 2014;

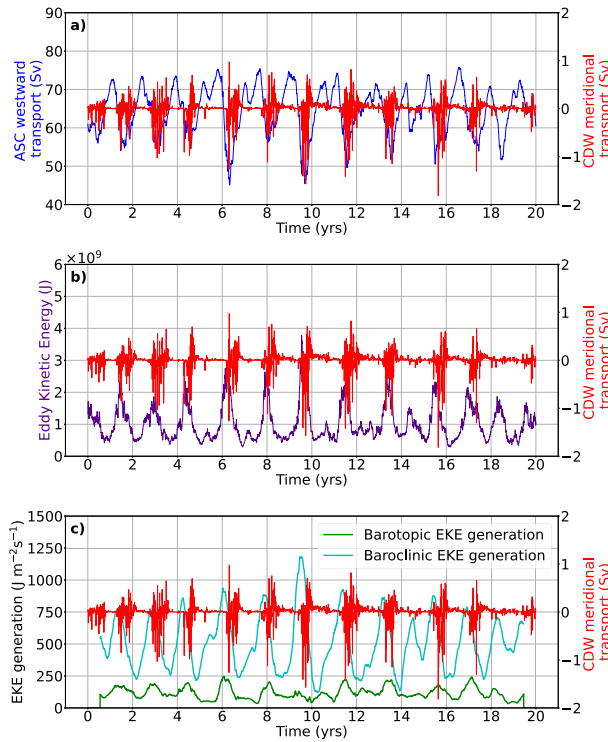


FIG. 6. (a) Time series of ASC strength and meridional volume transport of CDW onto shelf at latitude $y = -100$ km. (b) Time series of EKE per unit area and the same CDW transport time series as in (a). (c) Time series of baroclinic and barotropic energy conversions per unit area and the same CDW transport time series as in (a). Energy conversions are calculated as a rolling average of 200 days. All time series are for 20 years after the flow has equilibrated. The episodes of meridional CDW transport coincide with the weakening of the ASC and precede peaks in EKE and EKE generation by a short time lag of days.

[Stewart and Thompson 2015, 2016](#)). To determine if the CDW intrusions arise from eddies in the ASC, we compute the area-integrated eddy kinetic energy (EKE) in the ASC in the CDW layer. We use a layered thickness-weighted framework ([Young 2012](#)), with energy transfers between eddy energy reservoirs as described by [Aiki et al. \(2016\)](#) and [Yung et al. \(2022\)](#). The time-mean EKE in the i th layer is $(1/2)\rho_0 h_i |\mathbf{u}_i''|^2$, where ρ_0 is the reference density and we use the density of the top layer as the reference density, h_i is the thickness of layer i , \mathbf{u}_i is the velocity in layer i , and $\mathbf{u}_i'' = \mathbf{u}_i - \hat{\mathbf{u}}_i'$ is the deviation from the thickness-weighted mean velocity $\hat{\mathbf{u}}_i'$, where $\hat{\mathbf{u}}_i' = \overline{h_i \mathbf{u}_i' / h_i}$, with $\langle \cdot \rangle$ a time mean. The EKE is integrated over the ASC in the CDW layer, bounded by the latitudes of $y = -50$ km and $y = 100$ km and integrated across the whole channel in the zonal direction. Inspecting the time series of the EKE with the meridional volume transport of CDW in [Fig. 6b](#), plotted for 20 years at equilibrium, we observe that episodes of southward transport of CDW follow peaks in area-integrated EKE. The increased southward transport of CDW thus appears to be linked to a greater presence of eddies in the ASC, such that the temporal variability in rates of eddy generation could drive the intrusions of CDW.

To identify the mechanisms driving the temporal variability of EKE, we compute the baroclinic and barotropic contributions of energy conversion to EKE in the ASC ([Aiki et al. 2016; Yung et al. 2022](#)). The baroclinic energy conversion term, $\mathbf{u}_i' \cdot (\overline{h_i \nabla \phi_i'})$, links the contribution of interfacial form stress to EKE in layer i , while the barotropic energy conversion term, $\rho_0 (\mathbf{u}_i' \cdot \nabla) \cdot (\overline{h_i \mathbf{u}_i' \otimes \mathbf{u}_i'})$, is the contribution of Reynolds stress, and thus horizontal shear, to EKE. Here, ϕ_i is the Montgomery potential and $\phi_i' = \phi_i - \overline{\phi_i}$, where $\langle \cdot \rangle$ is a rolling mean over 200 days to smooth out transient eddy effects. The term $\mathbf{u}_i' = \mathbf{u}_i - \hat{\mathbf{u}}_i$ is the thickness-weighted mean velocity computed using a rolling mean, where $\hat{\mathbf{u}}_i = \overline{h_i \mathbf{u}_i / h_i}$, and \otimes is the outer product of two vectors.

The baroclinic and barotropic energy conversions for the control simulation of the widest canyon are plotted in [Fig. 6c](#) for 20 years at equilibrium. The peaks in both the baroclinic and barotropic energy conversions precede peaks in warm intrusions, showing that the generation of eddies results in more CDW intrusions with a short time lag of days. Crucially, the baroclinic energy conversion term dominates the barotropic energy conversion term, highlighting the contribution of baroclinic instability to the EKE gain. Hence, this baroclinic instability is the mechanism by which eddies are generated to drive CDW intrusions onto the shelf.

We conclude that episodic generation of eddies through baroclinic instability weakens the ASC, while simultaneously driving the onshore transport of CDW. A previous work by [Nakayama et al. \(2021\)](#) has already shown a link between a weak ASC and warm CDW intrusions, and in this channel model, a weaker ASC is linked with warm CDW intrusions by the generation of eddies through baroclinic instability. The mechanism is further supported by experiments with increased bottom drag, under which eddy generation is reduced and CDW intrusions are simultaneously inhibited (not shown). As the variability of CDW intrusions originates from changes in the generation of eddies in the ASC, the ASC is therefore a key governing factor of CDW intrusions whose intrinsic variability is crucial to be understood.

4. Intrinsic ASC variability

In [section 3](#), we demonstrated that there is an intrinsic time variability to CDW intrusions caused by a cycle of rising and falling rates of eddy generation in the ASC. However, we did not address the origin of the variability in the ASC. In this section, we show that the cycle of rates of eddy generation in the ASC can be explained using a low-order model, consisting of two nonlinear ordinary differential equations, that describes the coupling of available potential energy (APE) and eddy kinetic energy, and that the model predicts an intrinsically oscillatory ASC when linearized. We also compare the low-order model predictions to our isopycnal channel model simulations, first by comparing the energy evolution predicted by the low-order model to channel model simulations, followed by parameter sensitivity tests. These comparisons allow us to evaluate whether the physics of the low-order model can explain the key processes governing ASC time-variability in the fresh shelf regime.

a. Low-order model and oscillatory solution to linearized equations

We demonstrated that the intrinsic variability of the idealized ASC in the fresh shelf regime arises from eddy generation via baroclinic instability. However, the rate of baroclinic eddy generation is not constant even at equilibrium; instead, baroclinic instability occurs in a periodic cycle. The cause of this cycle and its time scale are unclear as there are no time-varying external forcings to induce this oscillatory behavior. Therefore, we aim to understand the equilibrated state better, prompting the use of a low-order model.

We postulate that the interannual variability in this system occurs due to energy exchange between total eddy energy and total available potential energy. To demonstrate this, we develop a low-order system that governs the evolution of total eddy energy, and total available potential energy in an idealized ASC, in order to understand the quasi-steady state of the ASC. We start with a two-layer, zonally symmetric isopycnal model of the ASC, pictured in Fig. 7, with constant zonal wind forcing. The fluid interface is assumed to have a constant slope. The energy budget of the system can be expressed as

$$\frac{dE}{dt} = \text{eddy energy conversion} - \text{damping}, \quad (2)$$

$$\frac{d\text{APE}}{dt} = \text{wind input} - \text{eddy energy conversion}, \quad (3)$$

with

$$E = \sum_i \int \left(\frac{1}{2} \rho_0 h_i |\mathbf{u}_i''|^2 + \frac{1}{2} \rho_0 g' \eta''^2 \right) dy, \quad (4)$$

$$\text{APE} = \sum_i \int \frac{1}{2} \rho_0 g' \eta^2 dy, \quad (5)$$

where E is the depth-integrated total eddy energy per unit length in the longitudinal direction and APE is the depth-integrated total available potential energy per unit longitudinal length. The term η , the isopycnal interface height, is defined relative to the initial interface height at the southern boundary and $\eta'' = \eta - \eta'$. Damping is in the form of λE , with λ being the linear damping coefficient. Eddy energy conversion is $|f|/N|\partial u/\partial z|E$ (following Marshall et al. 2017), where f is the Coriolis parameter, N is the buoyancy frequency, and u is the zonal velocity. Wind input per unit longitudinal length is given by $\int \boldsymbol{\tau} \cdot \mathbf{u}_{\text{surface}} dy$, where $\boldsymbol{\tau}$ is the wind stress vector and $\mathbf{u}_{\text{surface}}$ is the surface velocity.

We wish to express (2) and (3) as a coupled system of differential equations in terms of APE and E , so we define the components of the equation in terms of these variables. We assume geostrophic velocities in each of the isopycnal layers, thermal wind balance, rigid lid, constant linear shear, and zero bottom velocity. The zero bottom velocity is justified as bottom velocities in both our channel simulations and in observations around the East Antarctic are generally less than 10% of the surface velocities. The procedure for defining and discretizing these terms for the case of the two-layer model is outlined in the appendix, and we end up with the equations:

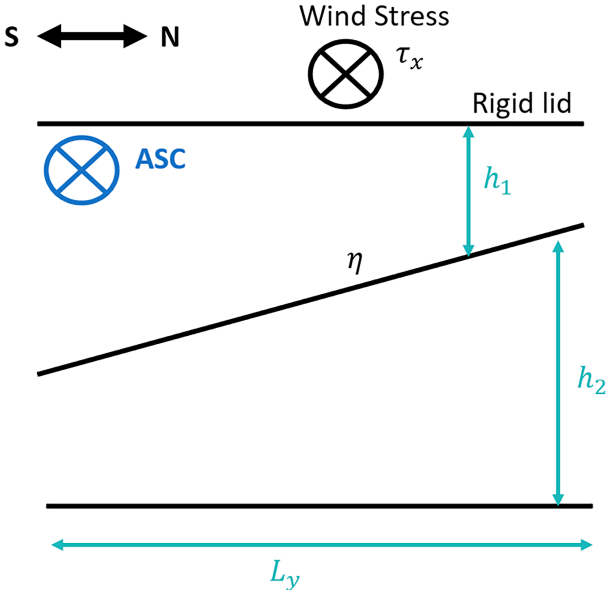


FIG. 7. Schematic showing features of the low-order model, replicating an ASC at equilibrium, with two density layers, a rigid lid, a sloping isopycnal of interface height η with a constant slope across the extent of the domain L_y , zonal wind stress input of τ_x , and layer thicknesses of each layer being h_1 and h_2 for top and bottom layers, respectively. The wind input slopes the isopycnal interface and spins up a westward current.

$$\frac{dE}{dt} = 2 \underbrace{\sqrt{\frac{6}{\rho_0 H L_y^3}}} \underbrace{\sqrt{\text{APE}}} - \lambda E, \quad (6)$$

$$\frac{d\text{APE}}{dt} = \underbrace{\frac{2|\tau_x|}{|f|} \sqrt{\frac{6g'}{\rho_0 L_y}}} \underbrace{\sqrt{\text{APE}}} - 2 \underbrace{\sqrt{\frac{6}{\rho_0 H L_y^3}}} \underbrace{\sqrt{\text{APE}}}, \quad (7)$$

where ρ_0 is the reference density, $g' = g\Delta\rho/\rho_0$ is the reduced gravity of the two-layer system, H is the total thickness of the fluid, L_y is the latitudinal extent of the domain where the slope of the density surface is constant, and τ_x is the zonal component of the wind stress input. We also use that for a two-layer model $N^2 = 2g'/H$.

Now, we have two coupled nonlinear ordinary differential equations [(6) and (7)]. To find the fixed points, we set $d/dt = 0$ and solve, setting the constants to a and b for simplicity. We get a nontrivial fixed point:

$$\sqrt{\text{APE}} = \lambda/a \quad \text{and} \quad E = b/a. \quad (8)$$

Upon linearizing the energy equations [(6) and (7)] about equilibrium (8), we obtain evolution equations for the deviations of E and APE about their equilibrium values. Combining these evolution equations, we end up with

$$\frac{d^2 E}{dt^2} = -\frac{ab}{2} E, \quad (9)$$

which has oscillatory solutions of the form $E \propto e^{i\omega t}$, with

$$\omega = \sqrt{\frac{ab}{2}} = \frac{1}{L_y} \sqrt{\frac{6|\tau_x|}{|f|\rho_0}} \left(\frac{2g'}{H} \right)^{1/4}, \quad (10)$$

$$T = \frac{2\pi}{\omega} = \pi L_y \sqrt{\frac{2\rho_0|f|}{3|\tau_x|}} \left(\frac{H}{2g'} \right)^{1/4}, \quad (11)$$

where ω is the radial frequency of oscillation and T is the period of the oscillation of E and APE.

The solution to the linearized equations about the fixed point is oscillatory, which is consistent with an intrinsically time-varying ASC. The oscillatory solution implies that the total eddy energy and available potential energy in the ASC will follow an oscillation with a steady period defined in (10), despite no time scale being imposed on the model through external forcing. The next section will compare the low-order model to the channel model simulations, such that conclusions about the underlying dynamics can be drawn between these systems.

b. Energy evolution in the low-order model

The low-order model [(6) and (7)] describes the evolution of eddy energy and available potential energy in a current system, and when the system is close to equilibrium, the low-order model acts as an oscillator. To evaluate the extent to which the low-order model replicates the physics in the isopycnal channel model simulations, we compare key characteristics of the low-order model to the simulations. We solve the low-order model fully to obtain the time evolution of energy reservoirs, starting from prescribed initial conditions. The predicted energy evolutions can then be compared to their corresponding quantities in the isopycnal channel model simulations.

Although the linearized low-order model does show an oscillation consistent with the channel model simulations, there are a number of assumptions in the low-order model that do not hold in the simulation, making direct comparisons difficult. For example, the low-order model assumes a constant slope of the density interface throughout the slope current and a linear drag, while the isopycnal channel simulations have a varying interfacial slope and quadratic drag. Additionally, the simulations feature continental slope topography, which can suppress the generation of eddies (Isachsen 2011), while the low-order model assumes a flat-bottom channel. The lack of topographic variation in the low-order model implies that all wind stress inputs have to be balanced by bottom drag, rather than being balanced by topographic form stress in a setup with bathymetric features (Munk and Palmén 1951). Hence, if both setups were to have similar equilibrated zonal transport values, then the low-order model would require much higher values of drag as it does not have any other way to dissipate zonal momentum. Expecting high values of λ in the low-order model, we choose $\lambda = 5 \times 10^{-7} \text{ s}^{-1}$ as this gives us energy values comparable to the control simulation in Fig. 8, and we use this bottom drag parameter to solve the nonlinear energy equations of the low-order model.

Solving the initial value problem for the nonlinear energy equations in (6) and (7) using the chosen bottom drag parameter, we find that the theoretical solution for E and APE from the low-

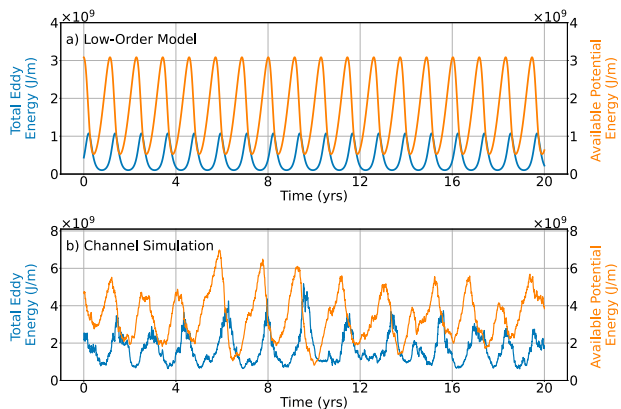


FIG. 8. (a) Solutions to the initial value problem of the low-order model, using $\lambda = 5 \times 10^{-7} \text{ s}^{-1}$ and initial conditions for E and APE, are 1.05 times and 2 times their equilibrium values in (8), respectively. (b) Diagnostics of eddy energy and available potential energy, calculated using 20 years of data at equilibrium from the control channel simulation (widest 200-km steep-sided canyon). The E is calculated in the CDW layer, and APE is calculated at the interface between the CDW layer and the lower surface water layer in the channel model simulations. Although the time series has a period greater than that predicted around the equilibrium state using the low-order model, the APE similarly peaks and declines before E begins to increase as eddies are being generated.

order model (Fig. 8a) is comparable to the E and APE time series calculated from the experimental data (Fig. 8b). The chosen initial conditions for E and APE are 1.05 times and 2 times their equilibrium values in (8), respectively, which are representative of the channel model simulations as the maximum APE in the control simulation is double the equilibrium APE. In the low-order model solutions, APE increases before E and begins to drop off once E starts to increase. This is similar behavior to that seen in the channel model simulations, where APE gain precedes the increase in E as plotted in Fig. 8b, supporting the mechanism that APE is being converted into eddy energy via baroclinic instability. A discrepancy between the solution to the initial value problem and the time series of energies from channel model simulations is the period of the oscillation. Although both plots in Fig. 8 show a cycle of regular oscillations, the period of oscillation in the channel model simulations is longer than that expected from the low-order model. Later, in this section, we show that the period of oscillation predicted by the low-order model is consistently shorter than that in the channel model simulations, and we also investigate the trends in the period of oscillation as experimental parameters are varied.

c. Parameter sensitivity tests in the low-order model

Having evaluated the solutions to the low-order model, showing the time evolution of the eddy energy reservoirs, we now investigate how changing parameters affects the predictions of the low-order model. In particular, we look at how predictions for period and equilibrium energies scale with parameters relevant to a changing ASC and compare these predictions with the isopycnal channel model simulations. In the solution to the linearized energy equation [(10)], the frequency of the intrinsic oscillation is

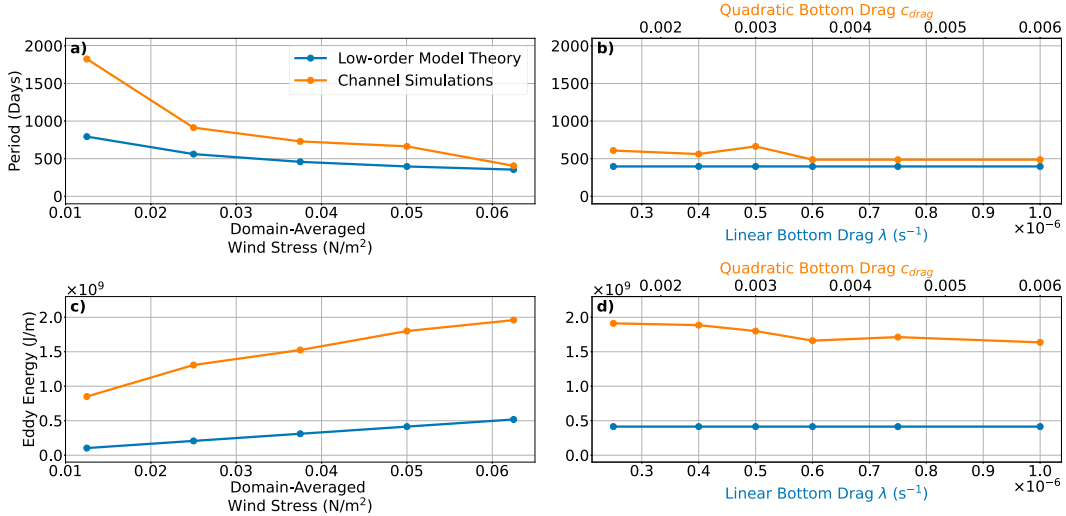


FIG. 9. Period of oscillation in E from the channel model simulations and in the low-order theory, with varying (a) wind stress and (b) bottom drag. The dominant frequency for each of the channel model simulations was selected from Fourier spectral analysis, and its period is plotted in orange, while the low-order model (10) used values from the channel model simulations to predict the period of oscillation (see Table 1). Magnitude of equilibrium of the total eddy energy from the channel model simulations and in the low-order theory, with varying (c) wind stress and (d) bottom drag.

proportional to $\sqrt{\tau_x}$ but independent of linear bottom drag λ . Additionally, the equilibrium energies in the low-order model (8), E_0 and APE_0 , are proportional to wind stress input τ_x and bottom drag squared λ^2 . Testing the parameter sensitivity of the channel model simulation as informed by the low-order model is significantly simpler and allows us to assess how the oscillation in the simulated ASC is affected by changing environmental conditions, hence focusing on the effect of wind stress and bottom drag.

We modify wind stress and bottom drag in our isopycnal channel model of the fresh shelf regime to test the dependence of the oscillation period and equilibrium energies on these parameters and verify the energy equations of the low-order model. We conducted four additional simulations for wind stress, at $\tau_0 = 0.025, 0.05, 0.075, 0.125 \text{ N m}^{-2}$, and five for bottom drag, with the quadratic drag coefficient at $c_{\text{drag}} = 0.0015, 0.0024, 0.0036, 0.0045, 0.006$, corresponding to a halving, 20% decrease, 20% increase, 50% increase, and doubling of the control simulation's bottom drag coefficient. All these simulations utilize the topography of the widest canyon in the control simulation shown in Fig. 1, as it exhibits the most regular periodic oscillation in ASC strength in our experiments and thus is the best comparison to the low-order model. A previous study by Stern et al. (2015) also showed an aperiodic cycle in an idealized jet, modeled on the Antarctic Circumpolar Current on the West Antarctic Peninsula continental shelf. However, we do not consider these simulations without a canyon, as preliminary experiments without a canyon did not reveal any regular oscillatory behavior in ASC strength. Understanding how an oscillation in ASC strength is induced uniquely on a continental slope with a canyon will be the subject of future work.

According to linear stability analysis of the low-order model equilibrium, the oscillation period is expected to decrease as wind stress is increased, but it is independent of bottom drag. Fourier

spectral analysis was conducted on the eddy kinetic energy time series in each channel model simulation. The dominant frequency was selected, and its period is plotted in orange for each of the channel model simulations in Fig. 9, with Fig. 9a for simulations varying wind stress and Fig. 9b for simulations varying bottom drag. The period predicted by the low-order model (10) is shown in blue, and we have substituted values from the channel model simulations to estimate the period and conduct the parameter sensitivity tests (see Table 1). We find that the period in the channel model simulations decreases as the strength of the wind forcing increases, but it is independent of bottom drag, as predicted by the linearization of the low-order model. The channel model simulations show a period systematically greater than that in the low-order model, with an example shown in Fig. 8 where the control simulation has a longer oscillation period in energy than in the low-order model. Regardless, the trends in the period of oscillation seen in the low-order model still hold in the channel model simulations as wind stress and bottom drag are varied (Figs. 9a,b).

TABLE 1. Experimental parameters used in the low-order model.

Parameter	Value
τ_x	0.05 N m^{-2} [domain average of (1)]
H	3000 m
ρ_0	1027.8 kg m^{-3}
$\Delta\rho$	0.5 kg m^{-3}
L_y	25 km
h_1	500 m
h_2	2500 m
N	$9.54 \times 10^{-4} \text{ s}^{-1}$
λ	$5 \times 10^{-7} \text{ s}^{-1}$

In addition to the period of E and APE oscillations, the low-order model parameters can also be used to predict the equilibrium values of E and APE and how they behave as wind stress and bottom drag are varied. From the low-order model, the theoretical equilibrium values of the E and APE, E_0 , and APE_0 , are proportional to the wind stress input τ_x and the square of the bottom drag λ^2 , respectively, as in (8). The equilibrium energy values in the channel model simulation were found by taking a spatial and time mean over 20 years of daily data over the continental shelf where the ASC is located, and the comparison between experimental and theoretical E_0 as wind and bottom drag are varied is shown in Figs. 9c and 9d, with the theoretical equilibrium eddy energy from the low-order model plotted in blue and the channel model simulation results plotted in orange. We see that as τ_x is increased, E_0 for channel model simulations increases in magnitude, matching the prediction by the low-order model. Channel model simulations have a decreasing magnitude of E_0 by 10% over a tripling of bottom drag, while the low-order model predicts that E_0 will remain constant. The equilibrium APE_0 in simulations have also been compared with the low-order model prediction (not shown), but the trends in theoretical APE_0 and those from the channel simulations do not align.

These discrepancies in equilibrium energies between the low-order model and channel model simulations are significant and could be due to a number of the assumptions in the low-order model, such as 1) the channel model simulations use a quadratic drag, while the low-order model uses a linear drag, as addressed earlier in the section; 2) the assumption that the rate of eddy energy generation is directly proportional to eddy energy, and vertical shear is an oversimplification; and 3) the low-order model assumes a flat-bottom channel, while the channel model simulations have a continental slope. These could contribute to the difference in trends seen in Fig. 9d and equilibrium APE_0 . Considering that the effect of the continental slope is excluded from the low-order model, the parallels between the low-order model and the channel model simulations already illustrate key similarities between the systems, especially in the trend in the period of oscillation as wind stress and bottom drag are varied.

Comparisons between the low-order model and the channel model simulations indicate that these systems share similar underlying dynamics, allowing us to draw comparisons. Both systems exhibit energy exchanges between APE and E , with APE acting as the source of energy for E , as enhanced eddy activity acts to flatten the isopycnals. This cycle of APE gain and loss drives the temporal variability of E and the ASC strength. The time scale of this energy exchange is independent of the time scale of external forcings, as the low-order model and the simulated ASC have constant wind forcing applied to the system. The low-order model therefore highlights the intrinsic oscillation in the ASC, where wind forcing and baroclinic instability dominate in turn, as illustrated in Fig. 10. Wind forcing acts to increase the APE of the current system by strengthening the ASC, while baroclinic instability dissipates the APE by converting it into eddy energy, with their equal contribution explaining the oscillatory behavior of the simulated ASC system in the fresh shelf regime.

5. Discussion and conclusions

We develop an idealized configuration of the ASC in a fresh shelf regime to demonstrate that canyons play a key role in the episodic cross-slope transport of warm CDW water. A cycle of rising and falling rates of eddy generation leads to a temporal variability in ASC strength and eddy kinetic energy in the flow. This temporal variability in eddy energy and ASC strength allows for episodic CDW intrusions onto the continental shelf via canyons, as a weakened current results in an up tilt of isopycnals, facilitating the transport of eddies and CDW onto the continental shelf. We also assess the importance of canyon width on CDW transport in our idealized channel simulations with a constant wind forcing; wider canyons allow for a greater transport of CDW onto the shelf with distinct episodes of intrusion at a regular frequency, while narrower canyons result in greater asymmetry between the draining and isolated pulses of warm CDW intrusions onto the shelf.

We additionally find that the temporal variability of CDW intrusions and the ASC is intrinsic to the idealized ASC system, as it is present even in this model with constant external forcings. The intrinsic variability exists as a consequence of the feedbacks between wind energy input and eddy generation. This relationship is supported by a low-order model of the ASC, which exhibits similar behavior to the isopycnal channel model simulations. In the low-order model, an intrinsic temporal variability in the current system is set up, as a regular cycle of energy gain and loss occurs. Available potential energy is converted to eddy energy and dissipated as the ASC becomes baroclinically unstable, but potential energy is generated as wind forcing continues to act on the system and spins up a strong current again, restarting the cycle, as illustrated in Fig. 10. The result that baroclinic instability is the dominant cause of variability in the modeled ASC comes with a caveat; this is an idealized model with constant forcings and thus does not impose any variability or other water mass transformations. Hence, baroclinic instability may play a different role in the variability of CDW intrusions seen in more realistic models and in observations.

There are currently few realistic modeling studies or observations of the ASC in the East Antarctic, which limits our understanding of the intrinsic variability in the ASC system. In regional models and observations, the presence of temporal variability across a range of time scales, irregular topography, and time-varying external forcings makes it difficult to isolate a dominant frequency of intrinsic oscillation in ASC strength. Additionally, both the surface-intensified and bottom-intensified slope currents are present in certain dense shelf regions of the East Antarctic, such as the Prydz Bay and downstream region. Therefore, our proposed mechanism driving an intrinsic variability in CDW intrusions and the ASC may not be directly applicable to these East Antarctic regions, as our isopycnal channel model and the low-order model are unable to simulate the bottom-intensified slope currents linked to dense shelf water export. However, further work could apply the physical understanding of the ASC, gained from using the low-order model, to realistic models and observations of the fresh shelf regions and diagnose the intrinsic variability that we see in the channel model simulations. New observation programs could also target longer periods of continuous measurements, such

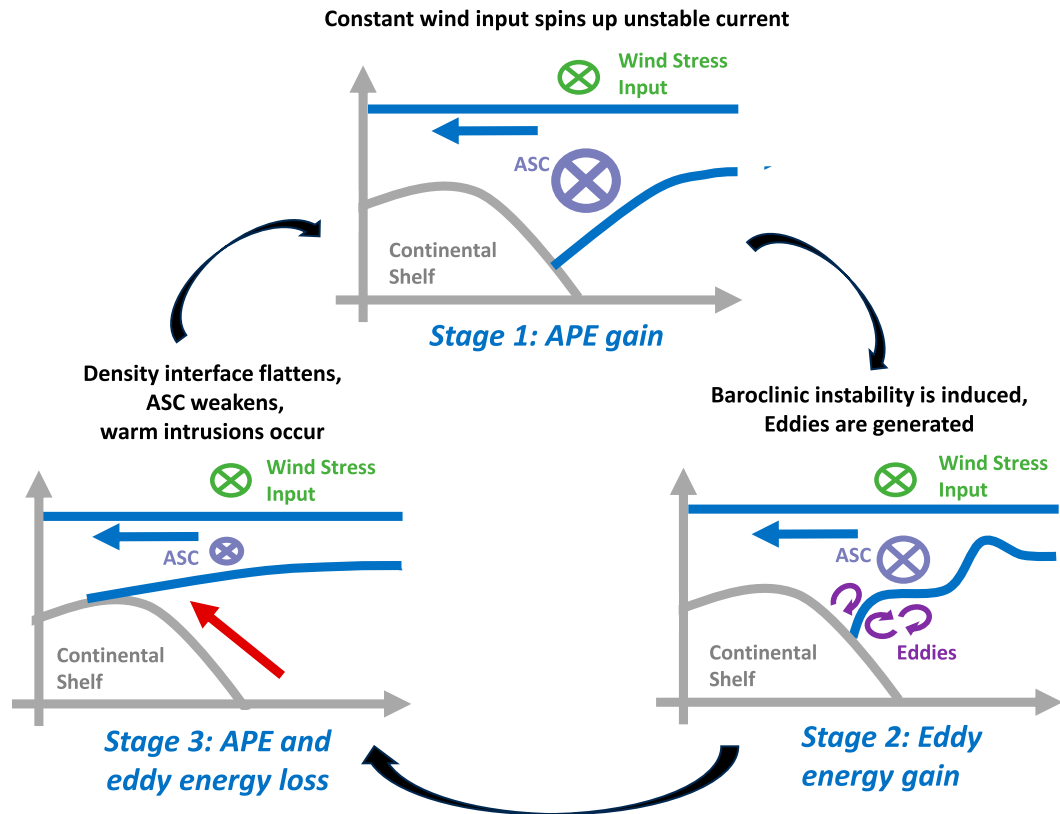


FIG. 10. Schematic illustrating the intrinsic oscillation of ASC strength over a canyon and its governing mechanisms. Stage 1: The constant wind stress input (green) spins up an unstable ASC (purple) through the Ekman transport of surface water and the steepening of isopycnals. Hence, APE is gained in the current system. Stage 2: Baroclinic instability generates eddies and results in a gain in eddy energy. Stage 3: The eddies flatten the density interface and weaken, slowing the ASC and shoaling the density surface on the continental shelf. A pathway for warm CDW to access the continental shelf is provided (red arrow), with the Ekman transport of surface water kept constant throughout the cycle (blue arrow).

that interannual variability in the ASC and CDW intrusions could be captured in observations. Observing and understanding this intrinsic variability can significantly improve our knowledge of how CDW intrusions in fresh shelf regions occur, which in turn would be important for predicting basal melt rates on the Antarctic continental shelf.

Although our idealized isopycnal channel simulations and low-order model capture the basic structure of the fresh shelf regime and the intrinsic oscillation of the ASC, there exist limitations to our study. For example, investigating the effect of varying canyon topography on cross-shelf dynamics, including the effects of canyon length, steepness of canyon slope, and continental slope (e.g., Isachsen 2011; Zhang et al. 2011; Stern et al. 2015; Bai et al. 2021; Si et al. 2022), was outside the scope of this study. The isopycnal channel simulation does not include sea ice and tides, nor the effects of water mass transformations (Stewart et al. 2019; Si et al. 2022, 2023). Hence, this isopycnal configuration cannot be used to address issues such as the effect of a freshened shelf via additional meltwater on the ASC (Moorman et al. 2020). Given the projected weakening of the coastal easterlies (Neme et al. 2022), assessing the impact of wind strength changes on CDW intrusions

around the East Antarctic using this isopycnal channel simulation is also an important area of future work. Additionally, the low-order model does not include a coupled effect between stratification and current width, where in channel model simulations, a narrower current is formed as stratification is reduced (not shown). Hence, to predict the period of the oscillation, the stratification and current width variables in the low-order model prediction in (10) both have to be modified as there are other compensating mechanisms present. The criterion required for this ASC oscillation to occur has also not been determined, but previous works in similar setups have pointed to the existence of a critical threshold for which periodic behavior in a jet can occur (Hogg and Blundell 2006; Chekroun et al. 2022). Understanding the criteria required and the experimental parameters that are key to inducing this oscillatory behavior in the ASC is a compelling area of future research and could also be applied to other boundary current systems around the globe.

Our idealized representation of the ASC captures a previously unknown feature of CDW intrusions and ASC strength, namely, their potential intrinsic temporal variability and the direct causal link between ASC weakening and CDW intruding onto the

continental shelf, via baroclinic instability and eddy generation. We conclude that a time-varying external forcing is not required to force interannual variability in ASC strength and CDW intrusions. There could thus be additional variability in CDW intrusions not captured in non-eddy-resolving models. Further work could assess the conditions required for the intrinsic variability to occur and diagnose this variability in realistic models and observations in an effort to improve our understanding of CDW intrusions around East Antarctica.

Acknowledgments. This research was supported by the Australian Research Council Special Research Initiative, Australian Centre for Excellence in Antarctic Science (ARC Project SR200100008). E. Q. Y. O. is supported by the Australian Government Research Training Program Scholarship (RTP). N. C. C. is supported by the Australian Research Council DECRA Fellowship DE210100749. A. McC. H. and M. H. E. (DP190100494) acknowledge funding from the Australian Research Council. This project received grant funding from the Australian Government as part of the Antarctic Science Collaboration Initiative program (ASCI00002). Computational resources were provided by the Australian National Computational Infrastructure at the ANU, which is supported by the Commonwealth Government of Australia. We thank the three anonymous reviewers for their constructive feedback that greatly improved the manuscript.

Data availability statement. Scripts used for analysis and for reproducing figures and the data used in figures are available at github.com/ongqingyee/idealised-ASC. The source code for the MOM6 simulation run is available on github.com/mom-ocean/MOM6.

APPENDIX

Derivation of Coupled Ordinary Differential Equations for Total Eddy Energy and Available Potential Energy in the Low-Order Model

We express the eddy budget in (2) and (3) in terms of the depth-integrated total available potential energy per unit longitudinal length, APE, and the depth-integrated total eddy energy per unit longitudinal length, E . We first define APE in this two-layered model (see Fig. 7). We have one free interface between the two fluid layers $\eta(y)$, a rigid lid, and define the thickness of each layer as h_i . We assume that the slope of the density interface is constant within the model domain, such that $\eta = \text{sgn}(\tau_x)\text{sgn}(f)sy$, where $s > 0$ is the magnitude of the slope of the density interface. The sign of the slope, $\partial\eta/\partial y$, depends on the sign of the wind stress and the Coriolis parameter. In a domain of latitudinal length L_y , over which the slope of the density surface is constant, the APE is

$$\begin{aligned} \text{APE} &= \int_0^{L_y} \frac{1}{2} \rho_0 g' \eta^2 dy \\ &= \frac{1}{6} \rho_0 g' s^2 L_y^3, \end{aligned} \quad (\text{A1})$$

where ρ_0 is the reference density and $g' = g\Delta\rho/\rho_0$ is the reduced gravity of the two-layer system.

Defining the eddy energy conversion term as $|f|/N|\partial u/\partial z|E$ (Marshall et al. 2012, 2017), where $E = \sum_i [(1/2)\rho_0 h_i |\mathbf{u}_i''|^2 + (1/2)\rho_0 g' \eta'^2] dy$, we can find an expression for this term using the parameters of the layered model. We can also use that for a two-layer model $N^2 = 2g'/H$. We approximate the vertical shear $\partial u/\partial z$ discretely as $\partial u/\partial z \approx (u_1 - u_2)/(H/2)$. Furthermore, by assuming constant linear shear and also zero bottom velocity $u_{\text{bot}} = 0$, we can integrate vertical shear up to get that the surface velocity is $u_{\text{surface}} = H\partial u/\partial z \approx 2(u_1 - u_2)$. To remove the velocity terms in each layer, we use the thermal wind balance $f(u_1 - u_2) = g'\partial\eta/\partial y = \text{sgn}(\tau_x)\text{sgn}(f)g's$ and combine all the terms above to write the expressions for the rate of change of depth-integrated eddy energy in terms of APE to arrive at (6).

Next, we define the rate of change of APE, the energy input from winds as $\int \int \tau \cdot \mathbf{u}_{\text{surface}} dA$. If we consider only the zonal flow component, the work per unit longitude is

$$\text{wind input} = \int \tau_x u_{\text{surface}} dy. \quad (\text{A2})$$

To express the wind energy input in terms of APE and E , we use the surface velocity $u_{\text{surface}} = 2(u_1 - u_2)$ and find the zonal velocities in individual layers through geostrophy to express the wind energy input in terms of the slope of the density interface:

$$u_{1g} = \frac{-1}{\rho_0 f} \frac{\partial p_{\text{atm}}}{\partial y}, \quad (\text{A3})$$

$$u_{2g} = -\frac{1}{\rho_0 f} \left(\frac{\partial p_{\text{atm}}}{\partial y} + g' \rho_0 \frac{\partial \eta}{\partial y} \right), \quad (\text{A4})$$

which when combined give

$$u_{\text{surface}} = 2(u_{1g} - u_{2g}) = \text{sgn}(\tau_x) \frac{2g's}{|f|}. \quad (\text{A5})$$

Substituting the expression for u_{surface} into (A2), using (A1) to write s in terms of APE, and using the same eddy energy conversion term as for (6), we end up with (7).

REFERENCES

- Adcroft, A., and Coauthors, 2019: The GFDL global ocean and sea ice model OM4.0: Model description and simulation features. *J. Adv. Model. Earth Syst.*, **11**, 3167–3211, <https://doi.org/10.1029/2019MS001726>.
- Aiki, H., X. Zhai, and R. J. Greatbatch, 2016: Energetics of the global ocean: The role of mesoscale eddies. *Indo-Pacific Climate Variability and Predictability*, S. K. Behera and T. Yamagata, Eds., World Scientific Series on Asia-Pacific Weather and Climate, Vol. 7, World Scientific, 109–134.
- Bai, Y., Y. Wang, and A. L. Stewart, 2021: Does topographic form stress impede prograde ocean currents? *J. Phys. Oceanogr.*, **51**, 2617–2638, <https://doi.org/10.1175/JPO-D-20-0189.1>.
- Boeira Dias, F., S. R. Rintoul, O. Richter, B. K. Galton-Fenzi, J. D. Zika, V. Pelichero, and P. Uotila, 2023: Sensitivity of simulated water mass transformation on the Antarctic shelf

- to tides, topography and model resolution. *Front. Mar. Sci.*, **10**, 1027704, <https://doi.org/10.3389/fmars.2023.1027704>.
- Chekroun, M. D., H. Dijkstra, T. Sengül, and S. Wang, 2022: Transitions of zonal flows in a two-layer quasi-geostrophic ocean model. *Nonlinear Dyn.*, **109**, 1887–1904, <https://doi.org/10.1007/s11071-022-07529-w>.
- Constantinou, N. C., and A. M. Hogg, 2019: Eddy saturation of the Southern Ocean: A baroclinic versus barotropic perspective. *Geophys. Res. Lett.*, **46**, 12 202–12 212, <https://doi.org/10.1029/2019GL084117>.
- Daae, K., T. Hattermann, E. Darelius, and I. Fer, 2017: On the effect of topography and wind on warm water inflow—An idealized study of the southern Weddell Sea continental shelf system. *J. Geophys. Res. Oceans*, **122**, 2622–2641, <https://doi.org/10.1002/2016JC012541>.
- , —, —, R. D. Mueller, K. A. Naughten, R. Timmermann, and H. H. Hellmer, 2020: Necessary conditions for warm inflow toward the Filchner Ice Shelf, Weddell Sea. *Geophys. Res. Lett.*, **47**, e2020GL089237, <https://doi.org/10.1029/2020GL089237>.
- Darelius, E., K. Makinson, K. Daae, I. Fer, P. R. Holland, and K. W. Nicholls, 2014: Hydrography and circulation in the Filchner Depression, Weddell Sea, Antarctica. *J. Geophys. Res. Oceans*, **119**, 5797–5814, <https://doi.org/10.1002/2014JC010225>.
- , I. Fer, and K. W. Nicholls, 2016: Observed vulnerability of Filchner-Ronne Ice Shelf to wind-driven inflow of warm deep water. *Nat. Commun.*, **7**, 12300, <https://doi.org/10.1038/ncomms12300>.
- DeConto, R. M., and D. Pollard, 2016: Contribution of Antarctica to past and future sea-level rise. *Nature*, **531**, 591–597, <https://doi.org/10.1038/nature17145>.
- Depoorter, M. A., J. L. Bamber, J. A. Griggs, J. T. M. Lenaerts, S. R. M. Ligtenberg, M. R. Van Den Broeke, and G. Moholdt, 2013: Calving fluxes and basal melt rates of Antarctic ice shelves. *Nature*, **502**, 89–92, <https://doi.org/10.1038/nature12567>.
- Fennel, W., and M. Schmidt, 1991: Responses to topographical forcing. *J. Fluid Mech.*, **223**, 209–240, <https://doi.org/10.1017/S0022112091001404>.
- Gudmundsson, G. H., F. S. Paolo, S. Adusumilli, and H. A. Fricker, 2019: Instantaneous Antarctic ice sheet mass loss driven by thinning ice shelves. *Geophys. Res. Lett.*, **46**, 13 903–13 909, <https://doi.org/10.1029/2019GL085027>.
- Gwyther, D. E., B. K. Galton-Fenzi, J. R. Hunter, and J. L. Roberts, 2014: Simulated melt rates for the Totten and Dalton ice shelves. *Ocean Sci.*, **10**, 267–279, <https://doi.org/10.5194/os-10-267-2014>.
- , T. J. O’Kane, B. K. Galton-Fenzi, D. P. Monselesan, and J. S. Greenbaum, 2018: Intrinsic processes drive variability in basal melting of the Totten Glacier Ice Shelf. *Nat. Commun.*, **9**, 3141, <https://doi.org/10.1038/s41467-018-05618-2>.
- Hattermann, T., L. H. Smedsrød, O. A. Nøst, J. M. Lilly, and B. K. Galton-Fenzi, 2014: Eddy-resolving simulations of the Fimbul Ice Shelf cavity circulation: Basal melting and exchange with open ocean. *Ocean Modell.*, **82**, 28–44, <https://doi.org/10.1016/j.ocemod.2014.07.004>.
- Herraiz-Borreguero, L., and A. C. Naveira Garabato, 2022: Poleward shift of Circumpolar Deep Water threatens the East Antarctic Ice Sheet. *Nat. Climate Change*, **12**, 728–734, <https://doi.org/10.1038/s41558-022-01424-3>.
- , J. A. Church, I. Allison, B. Peña-Molino, R. Coleman, M. Tomczak, and M. Craven, 2016: Basal melt, seasonal water mass transformation, ocean current variability, and deep convection processes along the Amery Ice Shelf calving front, East Antarctica. *J. Geophys. Res. Oceans*, **121**, 4946–4965, <https://doi.org/10.1002/2016JC011858>.
- Heywood, K. J., and B. A. King, 2002: Water masses and baroclinic transports in the South Atlantic and Southern oceans. *J. Mar. Res.*, **60**, 639–676, <https://doi.org/10.1357/002224002762688687>.
- , and Coauthors, 2014: Ocean processes at the Antarctic continental slope. *Philos. Trans. Roy. Soc.*, **A372**, 20130047, <http://doi.org/10.1098/rsta.2013.0047>.
- Hirano, D., and Coauthors, 2020: Strong ice-ocean interaction beneath Shirase Glacier Tongue in East Antarctica. *Nat. Commun.*, **11**, 4221, <https://doi.org/10.1038/s41467-020-17527-4>.
- Hogg, A. M. C., and J. R. Blundell, 2006: Interdecadal variability of the Southern Ocean. *J. Phys. Oceanogr.*, **36**, 1626–1645, <https://doi.org/10.1175/JPO2934.1>.
- Huneke, W. G. C., A. Klocker, and B. K. Galton-Fenzi, 2019: Deep bottom mixed layer drives intrinsic variability of the Antarctic Slope Front. *J. Phys. Oceanogr.*, **49**, 3163–3177, <https://doi.org/10.1175/JPO-D-19-0044.1>.
- , A. K. Morrison, and A. M. C. Hogg, 2022: Spatial and sub-annual variability of the Antarctic Slope Current in an eddy-ing ocean-sea ice model. *J. Phys. Oceanogr.*, **52**, 347–361, <https://doi.org/10.1175/JPO-D-21-0143.1>.
- , —, and —, 2023: Decoupling of the surface and bottom-intensified Antarctic Slope Current in regions of dense shelf water export. *Geophys. Res. Lett.*, **50**, e2023GL104834, <https://doi.org/10.1029/2023GL104834>.
- Isachsen, P. E., 2011: Baroclinic instability and eddy tracer transport across sloping bottom topography: How well does a modified Eady model do in primitive equation simulations? *Ocean Modell.*, **39**, 183–199, <https://doi.org/10.1016/j.ocemod.2010.09.007>.
- Kiss, A. E., and Coauthors, 2020: ACCESS-OM2 v1.0: A global ocean-sea ice model at three resolutions. *Geosci. Model Dev.*, **13**, 401–442, <https://doi.org/10.5194/gmd-13-401-2020>.
- Liu, C., Z. Wang, C. Cheng, R. Xia, B. Li, and Z. Xie, 2017: Modeling modified Circumpolar Deep Water intrusions onto the Prydz Bay continental shelf, East Antarctica. *J. Geophys. Res. Oceans*, **122**, 5198–5217, <https://doi.org/10.1002/2016JC012336>.
- , —, X. Liang, X. Li, X. Li, C. Cheng, and D. Qi, 2022: Topography-mediated transport of warm deep water across the continental shelf slope, East Antarctica. *J. Phys. Oceanogr.*, **52**, 1295–1314, <https://doi.org/10.1175/JPO-D-22-0023.1>.
- Marshall, D. P., J. R. Maddison, and P. S. Berloff, 2012: A framework for parameterizing eddy potential vorticity fluxes. *J. Phys. Oceanogr.*, **42**, 539–557, <https://doi.org/10.1175/JPO-D-11-048.1>.
- , M. H. P. Ambaum, J. R. Maddison, D. R. Munday, and L. Novak, 2017: Eddy saturation and frictional control of the Antarctic Circumpolar Current. *Geophys. Res. Lett.*, **44**, 286–292, <https://doi.org/10.1002/2016GL071702>.
- McMahon, C. R., and Coauthors, 2023: Southern Ocean pinnipeds provide bathymetric in-sights on the East Antarctic continental shelf. *Commun. Earth Environ.*, **4**, 266, <https://doi.org/10.1038/s43247-023-00928-w>.
- Moorman, R., A. K. Morrison, and A. M. C. Hogg, 2020: Thermal responses to Antarctic ice shelf melt in an eddy-rich global ocean-sea ice model. *J. Climate*, **33**, 6599–6620, <https://doi.org/10.1175/JCLI-D-19-0846.1>.
- Morlighem, M., and Coauthors, 2020: Deep glacial troughs and stabilizing ridges unveiled beneath the margins of the Antarctic ice sheet. *Nat. Geosci.*, **13**, 132–137, <https://doi.org/10.1038/s41561-019-0510-8>.
- Morrison, A. K., A. M. C. Hogg, M. H. England, and P. Spence, 2020: Warm Circumpolar Deep Water transport toward

- Antarctica driven by local dense water export in canyons. *Sci. Adv.*, **6**, eaav2516, <https://doi.org/10.1126/sciadv.aav2516>.
- Munk, W. H., and E. Palmén, 1951: Note on the dynamics of the Antarctic Circumpolar Current. *Tellus*, **3**, 53–55, <https://doi.org/10.3402/tellusa.v3i1.8609>.
- Nakayama, Y., and Coauthors, 2021: Antarctic Slope Current modulates ocean heat intrusions towards Totten Glacier. *Geophys. Res. Lett.*, **48**, e2021GL094149, <https://doi.org/10.1029/2021GL094149>.
- Neme, J., M. H. England, and A. M. C. Hogg, 2022: Projected changes of surface winds over the Antarctic continental margin. *Geophys. Res. Lett.*, **49**, e2022GL098820, <https://doi.org/10.1029/2022GL098820>.
- Nitsche, F. O., D. Porter, G. Williams, E. A. Cougnon, A. D. Fraser, R. Correia, and R. Guerrero, 2017: Bathymetric control of warm ocean water access along the East Antarctic Margin. *Geophys. Res. Lett.*, **44**, 8936–8944, <https://doi.org/10.1002/2017GL074433>.
- NOAA National Geophysical Data Center, 2009:ETOPO1 1 arc-minute global relief model. NOAA National Centers for Environmental Information, accessed 20 June 2022, <https://doi.org/10.7289/V5C8276M>.
- Nøst, O. A., M. Biuw, V. Tverberg, C. Lydersen, T. Hattermann, Q. Zhou, L. H. Smedsrød, and K. M. Kovacs, 2011: Eddy overturning of the Antarctic Slope Front controls glacial melting in the Eastern Weddell Sea. *J. Geophys. Res.*, **116**, C11014, <https://doi.org/10.1029/2011JC006965>.
- Ohshima, K. I., and Coauthors, 2013: Antarctic Bottom Water production by intense sea-ice formation in the Cape Darnley polynya. *Nat. Geosci.*, **6**, 235–240, <https://doi.org/10.1038/ngeo1738>.
- Paolo, F. S., H. A. Fricker, and L. Padman, 2015: Volume loss from Antarctic ice shelves is accelerating. *Science*, **348**, 327–331, <https://doi.org/10.1126/science.aaa0940>.
- Peña-Molino, B., M. S. McCartney, and S. R. Rintoul, 2016: Direct observations of the Antarctic Slope Current transport at 113°E. *J. Geophys. Res. Oceans*, **121**, 7390–7407, <https://doi.org/10.1002/2015JC011594>.
- Ribeiro, N., L. Herraiz-Borreguero, S. R. Rintoul, C. R. McMahon, M. Hindell, R. Harcourt, and G. Williams, 2021: Warm modified Circumpolar Deep Water intrusions drive ice shelf melt and inhibit Dense Shelf Water formation in Vincennes Bay, East Antarctica. *J. Geophys. Res. Oceans*, **126**, e2020JC016998, <https://doi.org/10.1029/2020JC016998>.
- Rignot, E., J. Mouginot, B. Scheuchl, M. Van Den Broeke, M. J. Van Wessem, and M. Morlighem, 2019: Four decades of Antarctic Ice Sheet mass balance from 1979–2017. *Proc. Natl. Acad. Sci. USA*, **116**, 1095–1103, <https://doi.org/10.1073/pnas.1812883116>.
- Rintoul, S. R., A. Silvano, B. Peña-Molino, E. van Wijk, M. Rosenberg, J. S. Greenbaum, and D. D. Blankenship, 2016: Ocean heat drives rapid basal melt of the Totten Ice Shelf. *Sci. Adv.*, **2**, e1601610, <https://doi.org/10.1126/sciadv.1601610>.
- Si, Y., A. L. Stewart, and I. Eisenman, 2022: Coupled ocean/sea ice dynamics of the Antarctic Slope Current driven by topographic eddy suppression and sea ice momentum redistribution. *J. Phys. Oceanogr.*, **52**, 1563–1589, <https://doi.org/10.1175/JPO-D-21-0142.1>.
- , —, and —, 2023: Heat transport across the Antarctic Slope Front controlled by cross-slope salinity gradients. *Sci. Adv.*, **9**, eadd7049, <https://doi.org/10.1126/sciadv.add7049>.
- Silvano, A., S. R. Rintoul, B. Peña-Molino, W. R. Hobbs, E. Van Wijk, S. Aoki, T. Tamura, and G. D. Williams, 2018: Freshening by glacial meltwater enhances melting of ice shelves and reduces formation of Antarctic Bottom Water. *Sci. Adv.*, **4**, eaap9467, <https://doi.org/10.1126/sciadv.aap9467>.
- , —, K. Kusahara, B. Peña-Molino, E. Van Wijk, D. E. Gwyther, and G. D. Williams, 2019: Seasonality of warm water intrusions onto the continental shelf near the Totten Glacier. *J. Geophys. Res. Oceans*, **124**, 4272–4289, <https://doi.org/10.1029/2018JC014634>.
- St-Laurent, P., J. M. Klinck, and M. S. Dinniman, 2013: On the role of coastal troughs in the circulation of warm Circumpolar Deep Water on Antarctic shelves. *J. Phys. Oceanogr.*, **43**, 51–64, <https://doi.org/10.1175/JPO-D-11-0237.1>.
- Stern, A., L.-P. Nadeau, and D. Holland, 2015: Instability and mixing of zonal jets along an idealized continental shelf break. *J. Phys. Oceanogr.*, **45**, 2315–2338, <https://doi.org/10.1175/JPO-D-14-0213.1>.
- Stewart, A. L., and A. F. Thompson, 2015: Eddy-mediated transport of warm Circumpolar Deep Water across the Antarctic Shelf Break. *Geophys. Res. Lett.*, **42**, 432–440, <https://doi.org/10.1002/2014GL062281>.
- , —, 2016: Eddy generation and jet formation via dense water outflows across the Antarctic continental slope. *J. Phys. Oceanogr.*, **46**, 3729–3750, <https://doi.org/10.1175/JPO-D-16-0145.1>.
- , —, A. Klocker, and D. Menemenlis, 2019: Acceleration and overturning of the Antarctic Slope Current by winds, eddies, and tides. *J. Phys. Oceanogr.*, **49**, 2043–2074, <https://doi.org/10.1175/JPO-D-18-0221.1>.
- Stokes, C. R., and Coauthors, 2022: Response of the East Antarctic Ice Sheet to past and future climate change. *Nature*, **608**, 275–286, <https://doi.org/10.1038/s41586-022-04946-0>.
- Thompson, A. F., K. J. Heywood, S. Schmidtko, and A. L. Stewart, 2014: Eddy transport as a key component of the Antarctic overturning circulation. *Nat. Geosci.*, **7**, 879–884, <https://doi.org/10.1038/ngeo2289>.
- , A. L. Stewart, P. Spence, and K. J. Heywood, 2018: The Antarctic Slope Current in a changing climate. *Rev. Geophys.*, **56**, 741–770, <https://doi.org/10.1029/2018RG000624>.
- Williams, G. D., S. Aoki, S. S. Jacobs, S. R. Rintoul, T. Tamura, and N. L. Bindoff, 2010: Antarctic bottom water from the Adélie and George V Land coast, East Antarctica (140–149°E). *J. Geophys. Res.*, **115**, C04027, <https://doi.org/10.1029/2009JC005812>.
- Williams, W. J., G. G. Gawarkiewicz, and R. C. Beardsley, 2001: The adjustment of a shelfbreak jet to cross-shelf topography. *Deep-Sea Res. II*, **48**, 373–393, [https://doi.org/10.1016/S0967-0645\(00\)00085-0](https://doi.org/10.1016/S0967-0645(00)00085-0).
- Young, W. R., 2012: An exact thickness-weighted average formulation of the Boussinesq equations. *J. Phys. Oceanogr.*, **42**, 692–707, <https://doi.org/10.1175/JPO-D-11-0102.1>.
- Yung, C. K., A. K. Morrison, and A. M. C. Hogg, 2022: Topographic hotspots of Southern Ocean eddy upwelling. *Front. Mar. Sci.*, **9**, 855785, <https://doi.org/10.3389/fmars.2022.855785>.
- Zhang, Y., J. Pedlosky, and G. R. Flierl, 2011: Shelf circulation and cross-shelf transport out of a bay driven by eddies from an open-ocean current. Part I: Interaction between a barotropic vortex and a steplike topography. *J. Phys. Oceanogr.*, **41**, 889–910, <https://doi.org/10.1175/2010JPO4496.1>.